

A 3D topological insulator quantum dot

Hari P. Paudel and Michael N. Leuenberger *

*NanoScience Technology Center and Department of Physics,
12424 Research Parkway Suite 400, Orlando, Florida 32826, United States*

3D topological insulators (TIs) are materials with topologically protected interface/surface states of massless Weyl fermions. This protection is manifested by the suppression of the backscattering caused by nonmagnetic impurities and edges on the surfaces¹⁻⁴ and by the robustness against any type of surface modifications. Consequently, 3D TI nanostructures are very interesting because of their large surface-to-volume ratio. The topological surface states in nanostructures exhibit a phase coherence length of several hundred nanometers^{11,12}. Experiments on both the physical and chemical synthesis of TI nanostructures were performed recently to understand their transport properties at the nanoscale²⁸⁻³⁰. Here we show the model of a quantum dot (QD) consisting of a spherical core-bulk heterostructure made of 3D TI materials, such as PbTe/Pb_{0.31}Sn_{0.69}Te, with bound massless and helical Weyl states existing at the interface and being confined in all three dimensions. The number of bound states can be controlled by tuning the size of the QD and the magnitude of the core and bulk energy gaps, which determine the confining potential. We demonstrate that such bound Weyl states can be realized for QD sizes of few nanometers. We identify the spin locking and the Kramers pairs, both hallmarks of 3D TIs. In contrast to topologically trivial semiconductor QDs, the confined massless Weyl states in 3D TI QDs are localized at the interface of the QD and exhibit a mirror symmetry in the energy spectrum. Because of the possibility to generate spin currents^{6,13,14}, the 3D TI QD opens up avenues to develop nanostructures for spintronics devices.

KEYWORDS: topological insulator, quantum dot, heterostructure.

3D topological insulators (TIs) are narrow-bandgap materials with topologically protected gapless (metallic) surface/interface states that appear within the bulk insulating gap^{1,2}. These states are characterized by the linear excitation energy of massless Weyl fermions. In such materials, the spins of the Kramers pairs are locked at a right angle to their momenta on the Fermi surface due to spin-orbit coupling. The surface states are protected by time reversal symmetry, making them robust against perturbation and exhibiting the characteristic suppression of backscattering from edges and nonmagnetic impurities¹⁻⁴. Unlike in normal metals with high disorder, where scattering is so strong that electrons get localized due to Anderson localization, on a topologically protected surface Anderson localization and backscattering are suppressed, resulting in ballistic and dissipationless charge transport. Such states are of great importance in low-power opto-spintronics that use spin currents under efficient electrical control^{5,6}. Decoherence can be circumvented by highly polarized spin states with helical spin texture⁷⁻¹⁰. The presence of the strong spin-orbit coupling on the surface of 3D TIs makes these materials excellent spin current generators.

The topological surface states in nanostructures have a phase coherence length of several hundred nanometers^{11,12}. Studies have been done to explore them as possible candidates for spin current generators in spintronics^{6,13,14}. Suppression of backscattering between states of opposite momentum and opposite spin was clearly observed in an experiment on a random alloy Bi_{1-x}Sb_x with strong atomic scale disorder¹⁵. This observation further confirms the potential use of 3D TIs for coherent spin transport phenomena.

The electronic properties of the surface states of 3D

TIs can be analyzed using Angle Resolved Photoemission Spectroscopy (ARPES)^{7,16-18} and scanning tunneling spectroscopy^{15,19}. Owing to their technological applications as well as fundamental concepts in solid state physics, these surface states, despite contributions coming from the conducting bulk band states^{20,21}, are probed and studied in the spin transport regime²². The surface states are probed in an experiment where the size of the Fermi surface measured by Shubnikov-de Haas oscillations are matched to the carrier density obtained in low-field Hall measurement²². In such experiments, application of a moderate to strong magnetic field reduces the conducting bulk bands' contribution to the conductivity. These attempts have been focused to get pure spin currents that have origin on the metallic surface states. To measure spin currents, TIs can be driven out of equilibrium by illuminating them with a circularly polarized light. The direction of the resulting photocurrents carried by helical Weyl fermions can be altered by changing the helicity of light from left circularly polarized to right circularly polarized light and vice versa^{23,24}.

An important feature of topological surfaces states is that they are robust against any type of surface modifications, in contrast to topologically trivial semiconductors where dangling bonds and reconstructions are common on the surfaces and modify largely their surface electronic properties. In 3D TI nanostructures the special properties of topologically protected surface states of TIs are very interesting because the large surface-to-volume ratio amplifies any physical effect originating from the surface. In such structures, the contribution to the conductivity from surface carriers is much greater than that from bulk crystals. In addition, the chemical potential can be electrically tuned using a gate voltage. For example, in an

interference type experiment such as Aharonov–Bohm (AB) oscillations^{25,26}, the coherent propagation of the Weyl electrons around the perimeter of a nanoribbon provides excellent evidence of the topological nature of the surface states in TI nanostructures¹². Experiments on both the physical and chemical synthesis of TI nanostructures have been done recently to understand their transport properties at the nanoscale^{27–29}. Recently, in a TI QD with tunable barriers based on ultrathin Bi₂Se₃ films, Coulomb blockade with >5 meV charging energy was observed and evidence of tunneling into excited states was provided³⁰.

So far, a theoretical study of electronic properties of 2D helical states occurring at the nanoscale of 3D TIs, such as in QDs, is still lacking. In this article, we present for the first time the study of bound Weyl states that are confined at the interface of a spherical core-bulk heterostructure QD made of 3D TI materials such as Pb_{1-x}Sn_xTe. We show that at the interface massless Weyl fermions are confined in all three dimensions. The directions of spin and momentum are tangent to the surface of the QD, as shown in Fig. 3. Remarkably, their inherent spin-momentum locking property exists even in the three-dimensional confinement of a QD. Since the massless Weyl fermions have a linear dispersion, there is a mirror symmetry in the energy spectrum between positive and negative energy states, in contrast to topologically trivial semiconductors where holes in p-type valence bands are typically heavier than electrons in s-type conduction bands, resulting in completely different energy spectra. We demonstrate that this symmetry in energy spectrum is preserved for the QD spectrum.

In Fig. 1 we show the model of our spherically symmetric 3D TI QD of a core-bulk structure with a single interface at radius $r = r_0$ [see Fig. 1 a]. This core-bulk structure consists, for example, of an inner core of PbTe and an outer bulk of Pb_{0.31}Sn_{0.69}Te with bandgaps of 0.187 and -0.187 eV, respectively, or vice versa, so that Weyl fermions are generated at the interface³¹. Here we used the bandgap formula provided in Ref. 32 for determining x . Note that the band crossing happens in Pb_{1-x}Sn_xTe at $x = 0.35$ at 4 K. The Weyl fermions are subjected to the spherically symmetric potential $\Delta(r)$ (Fig. 1 b), which breaks the translational invariance in radial direction.

To understand the energy spectrum and helical properties of massless Weyl fermions at the interface of a QD, we start with a Dirac Hamiltonian within the envelope function approximation. Neglecting the far band terms, we have

$$H = \begin{pmatrix} \Delta(\mathbf{r}) & \boldsymbol{\sigma} \cdot \hat{\mathbf{p}} \\ \boldsymbol{\sigma} \cdot \hat{\mathbf{p}} & -\Delta(\mathbf{r}) \end{pmatrix} \quad (1)$$

where $\boldsymbol{\sigma}$ are the Pauli matrices, $\hat{\mathbf{p}}$ is the momentum operator with Fermi velocities v_\perp and v_\parallel in angular and radial direction, respectively, $\Delta(\mathbf{r}) = \varepsilon_g(\mathbf{r})/2$ is the gap energy parameter. It is important to note that the spheri-

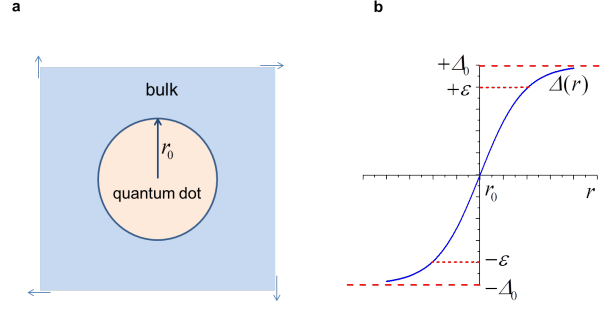


Figure 1: A heterostructure spherical core-bulk 3D TI QD with a single interface. **a.** The 2D interface of the 3D TIs can be curved to make a spherical core-bulk QD. Inner and outer materials are chosen in an appropriate ratio so that Weyl fermions are generated at the interface. The arrows at the corners are drawn to show the infinite size of the host. The core and bulk host can be chosen as PbTe and Pb_{0.31}Sn_{0.69}Te or vice versa. **b.** The potential $\Delta(r)$ with $\Delta(r - r_0) = -\Delta(r_0 - r)$ breaks the translational invariance of the crystal in radial direction. Weyl fermions possess zero mass; therefore, 3D TI QDs exhibit a mirror symmetry between positive and negative energy states. The energy of the bound interface states depends on the size of the QD and the strength of the potential. As an example, two bound states at the interface are shown with energies $+\varepsilon$ and $-\varepsilon$ (short dashed lines) for a QD of size $r_0 = 2$ nm.

cally symmetric $\Delta(r)$ breaks the translational invariance of the crystal in radial direction and has the symmetry $\Delta(r - r_0) = -\Delta(r_0 - r)$, where r_0 is the radius of the QD. The eigenfunctions of H are four-component spinors $\psi = \begin{bmatrix} \chi_- \\ \chi_+ \end{bmatrix}$, where χ_- and χ_+ are two-component spinors corresponding to the L_- and L_+ band, respectively, such as in Pb_{1-x}Sn_xTe. There are two important points: first, we assume our QD has spherical symmetry. This means the angular parts are separated from the radial part of the Dirac Hamiltonian given by equation (1). Second, in place of a constant mass term in the Dirac Hamiltonian, we have a spherically symmetric potential term $\Delta(r)$. Since this system has spherical symmetry, we follow the derivation of the solution for the central-force problem of a hydrogen atom in relativistic quantum mechanics, as treated explicitly in Ref. 33. After eliminating the angular parts, the radial part of the Dirac Hamiltonian given in equation (1) takes the form

$$H = \begin{pmatrix} \Delta(r) & -v_\parallel \hbar \left(\frac{d}{dr} - \frac{\kappa}{r} \right) \\ v_\parallel \hbar \left(\frac{d}{dr} + \frac{\kappa}{r} \right) & -\Delta(r) \end{pmatrix} \quad (2)$$

where $v_\parallel = 2.24 \times 10^5$ m/s for Pb_{1-x}Sn_xTe and $\kappa = \pm(j + \frac{1}{2})$ is a nonzero integer which can be positive or negative, j being the total angular momentum quantum number. For given κ , it is known from relativistic quantum mechanics that the angular momenta l_- and l_+ for χ_- and χ_+ are determined by the relations

$-\kappa = j(j+1) - l_-(l_-+1) + 1/4$ and $\kappa = j(j+1) - l_+(l_++1) + 1/4$, respectively. Now we solve the eigenvalue equation by squaring the Hamiltonian given by equation (2), resulting in the new eigenvalue equation $H^2\psi = \varepsilon^2\psi$, which consists of the two coupled second-order differential equations

$$\left(r^2 \frac{d^2}{dr^2} + 2r \frac{d}{dr}\right) f_{\mp} - (\lambda^2 r^2 + \kappa(\kappa \pm 1)) f_{\mp} = \beta r^2 \frac{d\Delta}{dr} f_{\pm} \quad (3)$$

where $f_{\pm} = r\chi_{\pm}$, $\beta = 1/v_{\parallel}\hbar$ and $\lambda = \beta\sqrt{(\Delta_0^2 - \varepsilon^2)}$. It is to be noted that the parameter λ behaves like a wave vector \mathbf{k} , whose allowed quantized values determine the particle's energy levels. The set of equations (3) are coupled inhomogeneous differential equations which can be solved by the standard Green's function technique. In a flat geometry, such as the thin layer of a 3D TI, the linear Weyl spectrum $k_{\perp} = 0$ is approximately equal to the soliton spectrum in the 1D Peierl's insulator and $\Delta(z)$ can be chosen to be $\Delta(z) = \Delta(\infty) \tanh(z/l)$.³⁴ The corresponding interface states are localized along the z -axis. Consequently, we adopt a similar potential along the radial direction of the form $\Delta(r') = \Delta_o \text{sgn}(r' - r_o)$, where Δ_o is the strength of the potential and r_o is the radius of the spherically symmetric interface of the QD. Hence, the source term in equation (3) is simply $\mathcal{F}(r') = 2\Delta_o\beta f_{\pm}(r_o)r'^2\delta(r' - r_o)$. The set of equations (3) can be solved by using the corresponding differential equation for the Green's function, i.e.

$$\left[\frac{d}{dr}\left(r^2 \frac{d}{dr}\right) - (\lambda^2 r^2 + \kappa(\kappa \pm 1))\right] G_{\mp} = \delta(r - r') \quad (4)$$

The solutions regular at $r = 0$ with outgoing wave behavior at $r \rightarrow \infty$ are the product of spherical modified Bessel functions of the order κ for G_- and of the order $\kappa - 1$ for G_+ , i.e. $G_-(r, r', \lambda) = C_- \mathcal{I}_{\kappa}(\lambda r_{<}) \mathcal{K}_{\kappa}(\lambda r_{>})$, $G_+(r, r', \lambda) = C_+ \mathcal{I}_{\kappa-1}(\lambda r_{<}) \mathcal{K}_{\kappa-1}(\lambda r_{>})$, where $r_{<}$ ($r_{>}$) is the smaller (larger) of r and r' . The functions $\mathcal{I}(\lambda r)$ and $\mathcal{K}(\lambda r)$ are, respectively, the first and the second kind of modified spherical Bessel functions, and C_{\mp} are the normalization constants. These constants are determined by the discontinuity in slope implied by the delta function in equation (4). Integration is performed at the interface of the QD along the radial direction: $\left[r^2 \frac{dG_{\mp}}{dr}\right]_{r'-\eta}^{r'+\eta} = 1$, where η is an infinitesimal quantity with $\eta > 0$. For $r = r' + \eta$, $r_{>} = r$, $r_{<} = r'$ and for $r = r' - \eta$, $r_{>} = r$, $r_{<} = r$. Consequently, the normalization constants are determined to be: $C_- = 1/\lambda r_o'^2 W_{\kappa}$ and $C_+ = 1/\lambda r_o'^2 W_{\kappa-1}$, where $W_{\kappa} = \left[\mathcal{I}_{\kappa}(\lambda r') \mathcal{K}'_{\kappa}(\lambda r) - \mathcal{I}'_{\kappa}(\lambda r) \mathcal{K}_{\kappa}(\lambda r')\right]_{r=r'}$ and $W_{\kappa-1} = \left[\mathcal{I}_{\kappa-1}(\lambda r') \mathcal{K}'_{\kappa-1}(\lambda r) - \mathcal{I}'_{\kappa-1}(\lambda r) \mathcal{K}_{\kappa-1}(\lambda r')\right]_{r=r'}$ are

the Wronskians of $\mathcal{I}(\lambda r)$ and $\mathcal{K}(\lambda r)$, respectively, for κ and $\kappa - 1$ order, and $\mathcal{I}'(\lambda r)$ and $\mathcal{K}'(\lambda r)$ are derivatives of the Bessel functions. The Wronskian of two linearly independent functions is proportional to $1/r^2$ for Sturm-Liouville type equations such as equation (4) (see Method A). The solutions of the inhomogeneous equations (3) are $f_{\mp} = \int G_{\mp}(r, r', \lambda) \mathcal{F}(r') dr' = 2\Delta_o\beta \int G_{\mp}(r, r', \lambda) f_{\pm} r'^2 \delta(r' - r_o) dr'$. Using the solutions for the Green's functions and integrating we obtain

$$f_- = 2\Delta_o\beta f_+ \mathcal{I}_{\kappa}(\lambda r_{<}) \mathcal{K}_{\kappa}(\lambda r_{>}) / \lambda W_{\kappa} \quad (5)$$

$$f_+ = 2\Delta_o\beta f_- \mathcal{I}_{\kappa-1}(\lambda r_{<}) \mathcal{K}_{\kappa-1}(\lambda r_{>}) / \lambda W_{\kappa-1} \quad (6)$$

where $r_{<}$ ($r_{>}$) is now the smaller (larger) of r and r_o . A transcendental equation is obtained by solving equations (5) and (6) and evaluating at $r = r_o$,

$$[z \mathcal{I}_{\kappa}(z) \mathcal{K}_{\kappa}(z)] [z \mathcal{I}_{\kappa-1}(z) \mathcal{K}_{\kappa-1}(z)] = 1/4 \Delta_o^2 \beta^2 r_o^2 \quad (7)$$

where $z = \lambda r_o$. Each term in the square bracket on the left hand side of equation (7) is a monotonically decreasing function of z (for $z > 0$), with maximum value of $1/(2\kappa + 1)$ for κ^{th} order term and $1/(2\kappa - 1)$ for $(\kappa - 1)^{th}$ order term occurring at $z = 0$ (see Method B). Therefore, their product has a maximum value of $1/(4\kappa^2 - 1)$ at $z = 0$ and is equal to $1/4 \Delta_o^2 \beta^2 r_o^2$. For $z \rightarrow \infty$, $[z \mathcal{I}_{\kappa}(z) \mathcal{K}_{\kappa}(z)] \rightarrow 1/2z$. In Fig. 2, we show the plot of equation (7) where the function $F(z)$ is defined as $F(z) = [z \mathcal{I}_{\kappa}(z) \mathcal{K}_{\kappa}(z)] [z \mathcal{I}_{\kappa-1}(z) \mathcal{K}_{\kappa-1}(z)]$. Since $F(z)$ is a monotonically decreasing function, for each κ , there is at most a single solution given by the intersection of $F(z)$ with the constant $1/4 \Delta_o^2 \beta^2 r_o^2$ (dashed line and solid line in Fig. 2). The critical limit for having a single solution is determined by the intersection at the maximum value of $F(z)$, which occurs at $z = 0$. This means that there exists a single solution of equation (7) for each κ as long as the condition $1/4 \Delta_o^2 \beta^2 r_o^2 \leq 1/(4\kappa^2 - 1)$ is satisfied. Fig. 2 shows the plot of the first three different values of κ , $\kappa = 1$ (red), 2 (blue) and 3 (pink), each a monotonically decreasing line (solid line) cut by a horizontal line (dashed line) at most one time. Since $\lambda = \beta\sqrt{(\Delta_0^2 - \varepsilon^2)}$, each single solution gives rise to two bound states with same magnitude but opposite sign of energy. Hence, if the Fermi energy is set at the origin where the bands cross, there is an electron-hole mirror symmetry in the energy spectrum. Indeed, this makes sense since Weyl fermions are massless at zero band gap with the linear dispersion relation. This result is in stark contrast to topologically trivial semiconductor QDs where holes are typically heavier than electrons and therefore break the electron-hole mirror symmetry in the energy spectrum.

As the size of the QD grows, it is filled with more and more bound states (see Fig. 2) where for smaller value

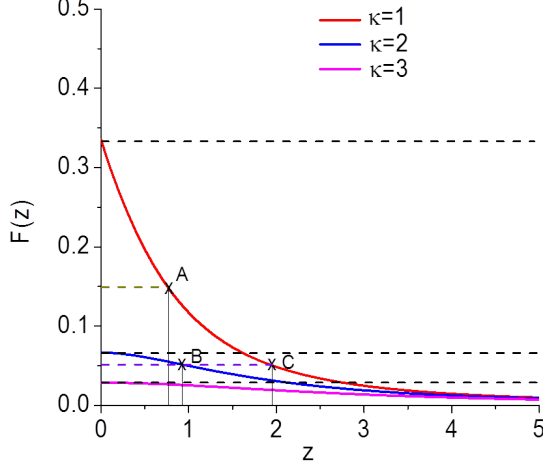


Figure 2: Plot of equation (7). The function $F(z)$ is defined as $F(z) = [z\mathcal{I}_\kappa(z)\mathcal{K}_\kappa(z)][z\mathcal{I}_{\kappa-1}(z)\mathcal{K}_{\kappa-1}(z)]$. Intersection of horizontal (black) dashed line and monotonically decreasing solid line at $z = 0$ gives the minimum threshold of the size of a QD to have two bound states, one positive and one negative energy state, for a given confining potential. For the larger size of the QD (smaller value of $F(z)$), multiple bound states are available, corresponding to multiple intersection points. As the size of the QD increases, the available positions of these bound states lie deep inside the confining potential well. The intersection points A, B and C are example points where we evaluate the wavefunctions. The energy of the bound states are determined by the relation $z = \lambda r_o$.

of $F(z)$, a horizontal dashed line makes multiple cuts at different values of the energy (i.e. z) for different κ . It is important to note that for negative κ , the solutions diverge at the origin and are therefore physically not valid. This result has profound implications because the sign of κ determines whether \mathbf{j} is parallel or antiparallel to the spin \mathbf{s} (see Ref. 33). Since κ is only allowed to be positive, only one spin orientation with respect to \mathbf{j} is permitted. This corresponds to the spin locking effect, which is a hallmark of 3D TIs (see Fig. 3). The condition $1/4\Delta_o^2\beta^2r_o^2 = 1/(4\kappa^2 - 1)$ determines the lower limit of the size of the QD to hold two bound interface states, a positive and a negative energy state, for a given value of the confining potential strength. The critical QD size depends on the Fermi velocities and band gaps of the 3D TI materials. In $\text{Pb}_{1-x}\text{Sn}_x\text{Te}$, the strength Δ_o of the confining potential can be taken as half of the band gap, by definition, of PbTe, which is 0.0935 eV. Taking the Fermi velocity on the surface to be $2.24 \times 10^5 \text{ m/s}$,³⁴ results in a critical QD size of $r_0 = 1.4 \text{ nm}$ for $\kappa = 1$ at $z = 0$. Similarly for $\kappa = 2$ at $z = 0$, the critical QD size for $\text{Pb}_{1-x}\text{Sn}_x\text{Te}$ is $r_0 = 3 \text{ nm}$. The energy of the bound states are determined from $z = \lambda r_o$, which gives a very shallow energy level of $\varepsilon = \pm\Delta_o$ for $z = 0$.

For a given value of κ , quantum numbers character-

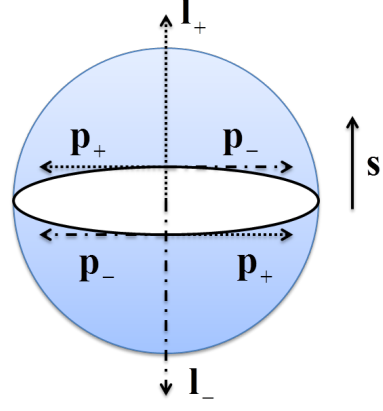


Figure 3: This schematic shows the partial momenta \mathbf{p}_- and \mathbf{p}_+ of the χ_- and χ_+ components on the surface of the QD which give rise to the angular momenta \mathbf{l}_- and \mathbf{l}_+ . In this visualization it is obvious that the spin \mathbf{s} is locked perpendicular to the momenta \mathbf{p}_- and \mathbf{p}_+ and perpendicular to the interface, which is a hallmark of 3D TIs.

χ_-			χ_+		
κ	l_-	j	κ	l_+	j
1	1	1/2	1	0	1/2
2	2	3/2	2	1	3/2
3	3	5/2	3	2	5/2
4	4	7/2	4	3	7/2

Table I: χ_- and χ_+ components

izing the wavefunctions χ_- and χ_+ can be determined. For $\kappa = 1, 2, 3$ and 4, the possible combination of the quantum numbers are shown in Table I for both spinors χ_- and χ_+ . Note that only the positive values of κ are shown since a negative κ is prohibited. Here we observe that the χ_- component is characterized by the spin being antiparallel to its angular momentum, whereas the χ_+ component is characterized by the spin being parallel to its angular momentum. We show now how to identify the Kramers pairs. According to Kramers theorem, which applies to a time-reversal invariant system, a spin 1/2 state is at least twofold degenerate on the surface of a 3D TI. Hence, using the 4-spinor notation $[|\chi_- \rangle, |\chi_+ \rangle]$, spin-orbit kets $|m_l, m_s \rangle$, and Clebsch-Gordan coefficients, we obtain the following examples of Kramers pairs. For $\kappa = 1$, a 4-spinor state $\left[\left(\sqrt{\frac{2}{3}} |1, -\frac{1}{2} \rangle - \sqrt{\frac{1}{3}} |0, \frac{1}{2} \rangle \right), |0, \frac{1}{2} \rangle \right]$ with $m_j = 1/2$ has a Kramers partner $\left[\left(\sqrt{\frac{1}{3}} |0, -\frac{1}{2} \rangle - \sqrt{\frac{2}{3}} |-1, \frac{1}{2} \rangle \right), |0, -\frac{1}{2} \rangle \right]$ with $m_j = -\frac{1}{2}$. For $\kappa = 2$, the 4-spinor states $\left[\left(\sqrt{\frac{4}{5}} |2, -\frac{1}{2} \rangle - \sqrt{\frac{1}{5}} |1, \frac{1}{2} \rangle \right), |1, \frac{1}{2} \rangle \right]$ with $m_j = \frac{3}{2}$ and $\left[\left(\sqrt{\frac{3}{5}} |1, -\frac{1}{2} \rangle - \sqrt{\frac{2}{5}} |0, \frac{1}{2} \rangle \right), \left(\sqrt{\frac{1}{3}} |1, -\frac{1}{2} \rangle + \sqrt{\frac{2}{3}} |0, \frac{1}{2} \rangle \right) \right]$ with $m_j = \frac{1}{2}$ have Kramers partners

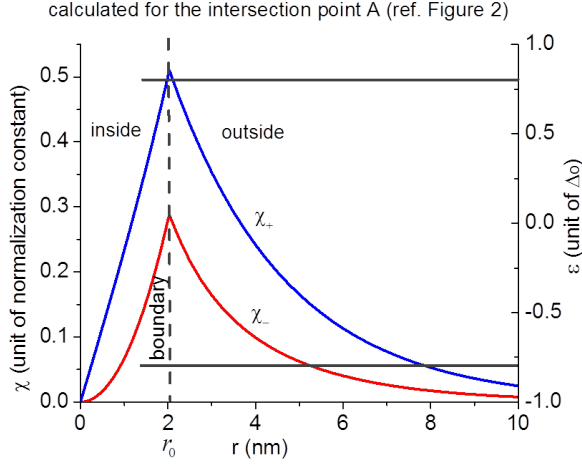


Figure 4: Spatial dependence of the two-component spinors χ_- and χ_+ inside and outside the QD calculated for the intersection point A shown in Fig. 2. The QD is made of PbTe/Pb_{0.31}Sn_{0.69}Te core-bulk heterostructure with a core of size $r_0 = 2$ nm. The vertical dashed line denotes the position of the QD boundary. The solid horizontal lines represent the energy eigenvalues $\varepsilon_{\pm} = \pm 0.8\Delta_o$, as marked on the right vertical axis.

$\left[\left(\sqrt{\frac{1}{5}} \left| -1, -\frac{1}{2} \right\rangle - \sqrt{\frac{4}{5}} \left| -2, \frac{1}{2} \right\rangle \right), \left| -1, -\frac{1}{2} \right\rangle \right]$
 with $m_j = -\frac{3}{2}$ and
 $\left[\left(\sqrt{\frac{2}{5}} \left| 0, -\frac{1}{2} \right\rangle - \sqrt{\frac{3}{5}} \left| -1, \frac{1}{2} \right\rangle \right), \left(\sqrt{\frac{2}{3}} \left| 0, -\frac{1}{2} \right\rangle + \sqrt{\frac{1}{3}} \left| -1, \frac{1}{2} \right\rangle \right) \right]$
 with $m_j = -\frac{1}{2}$, respectively. A state with $l_{\mp} = 2$ has two pairs of Kramers partner and a state with $l_{\mp} = 3$ has 3 pairs Kramers partner. In general, the number of Kramers pairs is determined by the spin multiplicity for each m_j value.

In Figs. 4 and 5 we show the spatial wavefunctions of the χ_- and χ_+ components inside and outside the QD made of the core-bulk heterostructure PbTe/Pb_{0.31}Sn_{0.69}Te. Figs. 4 shows the example of the intersection point A (see Fig. 2), and Fig. 5 shows the example of the intersection points B and C (see Fig. 2). Since the 4-spinors must be continuous at the boundary, also each of the 2-spinor components must be continuous, i.e. χ_-^{in} and χ_+^{in} must be equal to the spinors χ_-^{out} and χ_+^{out} , respectively, at the boundary of the QD surface. The horizontal solid and short dashed lines in Figs. 4 and 5 represent the energy eigenvalues, respectively, at the intersection point A, corresponding to a size of the QD of 2 nm, and at the intersection point B and C, corresponding to a size of the QD of 3.5 nm. Eigenvalues are given by $\varepsilon_{\pm} = \pm 0.80\Delta_o$ at point A, $\varepsilon_{\pm} = \pm 0.91\Delta_o$ at point B, and $\varepsilon_{\pm} = \pm 0.48\Delta_o$ at point C.

In conclusion, we have shown that Weyl fermions can be confined in all three dimensions at the spherically shaped interface between two narrow-bandgap semiconductor alloys, such as the core-bulk heterostructure made of PbTe/Pb_{0.31}Sn_{0.69}Te. This configuration provides us

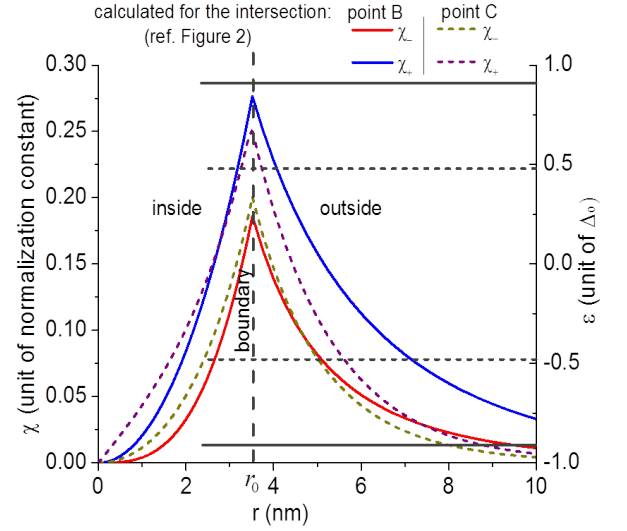


Figure 5: Spatial dependence of the two-component spinors χ_- and χ_+ inside and outside the QD calculated for the intersection points B and C shown in Fig. 2. The QD is made of PbTe/Pb_{0.31}Sn_{0.69}Te core-bulk heterostructure with a core of size $r_0 = 3.5$ nm. The vertical dashed line denotes the position of the QD boundary. The solid horizontal lines represent the energy eigenvalues $\varepsilon_{\pm} = \pm 0.91\Delta_o$ at point B and $\varepsilon_{\pm} = \pm 0.48\Delta_o$ at point C, as marked on the right vertical axis.

with the model of a spherical 3D TI QD with tunable size r_0 and potential Δ_0 , which allows for complete control over the number of bound interface states. In contrast to topologically trivial semiconductor QDs, the energy spectrum of the 3D TI QD exhibits a mirror symmetry between positive and negative energy states, which is typical for massless Weyl fermions. While in trivial semiconductor QDs the states are confined inside the core material, in a 3D TI QD the states are confined at the interface between the core and the bulk materials. We have shown that each of these bound states are characterized by the intrinsic spin-momentum locking property with helical spin states, which they inherit from the 2D interface structure. Therefore, 3D TI QDs have completely new physical properties, which might be very useful for the development of future spintronics devices due to their inherent topological protection against backscattering.

Acknowledgments

We acknowledge support from NSF (Grants ECCS-0901784 and Grant ECCS-1128597) and AFOSR (Grant FA9550-09-1-0450). M.N.L. thanks Daniel Loss for fruitful discussions during his stay at the University of Basel, Switzerland. M.N.L. acknowledges partial support from the Swiss National Science Foundation.

Methods

A. Calculation of the Wronskian

The Wronskian of the functions $\mathcal{I}_\kappa(z)$ and $\mathcal{K}_\kappa(z)$ is defined as³⁵

$$W_\kappa[\mathcal{I}_\kappa(z), \mathcal{K}_\kappa(z)] = \mathcal{I}_\kappa(z) \mathcal{K}'_\kappa(z) - \mathcal{I}'_\kappa(z) \mathcal{K}_\kappa(z), \quad (8)$$

where the prime denotes the derivative of the function. For independent solutions, it is to be noted that Wronskian is proportional to $1/p(x)$ in a Sturm-Liouville type equation $\frac{d}{dx} \left[p(x) \frac{dy}{dx} \right] + g(x)y = 0$. Therefore, Wronskians in the text are calculated to be

$$W_\kappa[\mathcal{I}_\kappa(z), \mathcal{K}_\kappa(z)] = -\frac{1}{z^2} \quad (9)$$

and

$$W_{\kappa-1}[\mathcal{I}_{\kappa-1}(z), \mathcal{K}_{\kappa-1}(z)] = -\frac{1}{z^2}. \quad (10)$$

B. Maximum of the function $F(z)$

The limiting forms of modified Bessel functions are given by

$$\left. \begin{aligned} I_\kappa(z) &= \frac{1}{\Gamma(\kappa+1)} \left(\frac{z}{2}\right)^\kappa \\ K_\kappa(z) &= \frac{\Gamma(\kappa)}{2} \left(\frac{2}{z}\right)^\kappa \end{aligned} \right\} \text{ as } z \rightarrow 0. \quad (11)$$

The modified spherical Bessel functions can be written in terms of modified Bessel functions as

$$\mathcal{I}_\kappa(z) = \left(\sqrt{\frac{\pi}{2z}}\right) I_{\kappa+\frac{1}{2}}(z), \quad \mathcal{K}_\kappa(z) = \left(\frac{2}{\pi z}\right) K_{\kappa+\frac{1}{2}}(z). \quad (12)$$

Therefore, the function

$$F(z) = [z\mathcal{I}_\kappa(z)\mathcal{K}_\kappa(z)][z\mathcal{I}_{\kappa-1}(z)\mathcal{K}_{\kappa-1}(z)] \quad (13)$$

has the limiting form $F(z) = \frac{1}{4\kappa^2-1}$ as $z \rightarrow 0$.

-
- * Electronic address: michael.leuener@ucf.edu
- ¹ Moore, J. E. The birth of topological insulators. *Nature* **464**, 194 (2010).
 - ² Hasan, M. Z. & Kane C. L. Colloquium: Topological insulators. *Rev. Mod. Phys.* **82**, 3045 (2010).
 - ³ Kane, C. L. & Mele, E. J. Z2 topological order and the quantum spin hall effect. *Phys. Rev. Lett.* **95**, 146802 (2005).
 - ⁴ Fu, L. & Kane, C. L. Topological insulators with inversion symmetry. *Phys. Rev. B* **76**, 045302 (2007).
 - ⁵ Zutic, I., Fabian, J. & Das Sarma, S. Spintronics: Fundamentals and applications. *Rev. Mod. Phys.* **76**, 323-345 (2004).
 - ⁶ Pesin, D. & MacDonald, A. H. Spintronics and pseudospintronics in graphene and topological insulators. *Nature Mater.* **11**, 409 (2012).
 - ⁷ Chen, Y. L., et al. Experimental Realization of a Three-Dimensional Topological Insulator, Bi₂Te₃. *Science* **325**, 178-181 (2009).
 - ⁸ Hsieh, D., et al. A tunable topological insulator in the spin helical Dirac transport regime. *Nature* **460**, 1101 (2009).
 - ⁹ Fu, L. & Kane, C. L. Superconducting proximity effect and Majorana Fermions at the surface of a topological insulator. *Phys. Rev. Lett.* **100**, 096407 (2008).
 - ¹⁰ Leek, P. J., et al. Observation of Berry's phase in a solid-state qubit. *Science* **318**, 1889-1892 (2007).
 - ¹¹ He, H.-T., et al. Impurity Effect on Weak Antilocalization in the Topological Insulator Bi₂Te₃. *Phys. Rev. Lett.* **106**, 166805 (2011).
 - ¹² Peng, H. L., et al. Aharonov-Bohm interference in topological insulator nanoribbons. *Nature Mater.* **9**, 225-229 (2010).
 - ¹³ Edelstein, V. M., Spin polarization of conduction electrons induced by electric current in two-dimensional asymmetric electron systems. *Solid State Commun.* **73**, 233-235 (1990).
 - ¹⁴ Wunderlich, J., Kaestner, B., Sinova, J. & Jungwirth, T. Experimental observation of the spin -Hall effect in a two-dimensional spin-orbit coupled semiconductor system. *Phys. Rev. Lett.* **94**, 047204 (2005).
 - ¹⁵ Roushan, P. et al. Topological surface states protected from backscattering by chiral spin texture. *Nature* **460**, 1106-1109 (2009).
 - ¹⁶ Hsieh, D. et al. A topological Dirac insulator in a quantum spin Hall phase. *Nature* **452**, 970-974 (2008).
 - ¹⁷ Hsieh, D. et al. Observation of unconventional quantum spin textures in topological insulators. *Science* **323**, 919-922 (2009).
 - ¹⁸ Xia, Y. et al. Observation of a large-gap topological-insulator class with a single Dirac cone on the surface. *Nature Phys.* **5**, 398-402 (2009).
 - ¹⁹ Alpichshev, Z. et al. STM imaging of electronic waves on the surface of Bi₂Te₃: topologically protected surface states and hexagonal warping effects. *Phys. Rev. Lett.* **104**, 016401 (2010).
 - ²⁰ Qu, D., Hor, Y. S., Xiong, J., Cava, R. J. & Ong, N. P. Quantum oscillations and Hall anomaly of surface states in the topological insulator Bi₂Te₃. *Science* **329**, 821824 (2010).
 - ²¹ Butch, N. P. et al. Strong surface scattering in ultrahigh-mobility Bi₂Se₃ topological insulator crystals. *Phys. Rev. B* **81**, 241301 (2010).
 - ²² Analytis, J. G. et al. Two-dimensional surface state in the quantum limit of a topological insulator. *Nature Physics*, **6**, 960- 964 (2010).
 - ²³ McIver, J. W. et al. Control over topological insulator photocurrents with light polarization. *Nature Nanotechnology* **7**, 96-100 (2012).
 - ²⁴ Hosur, P. Circular photogalvanic effect on topological insulator surfaces: Berry-curvature-dependent response. *Phys. Rev. B* **83**, 035309 (2011).
 - ²⁵ Aharonov, Y. & Bohm, D. *Phys. Rev.* **115**, 485 (1959).
 - ²⁶ Webb, S., Washburn, Umbach, C. P. & Laibowitz, R. B. *Phys. Rev. Lett.* **54**, 2696 (1985).
 - ²⁷ Cha, J. J., Koski, K. J. & Cui, Y. Topological in-

- ulator nanostructures. *Phys. Status Solidi (PRL)*. DOI 10.1002/pssr.201206393.
- ²⁸ Peng, H. et al. Topological insulator nanostructures for near-infrared transparent flexible electrodes. *Nature Chem.* **4**, 218-286 (2012).
 - ²⁹ Kong, D. & Cui, Y. Opportunities in chemistry and materials science for topological insulators and their nanostructures *Nature Chem.* **3**, 845-849 (2011).
 - ³⁰ Cho, S. et al. Topological Insulator Quantum Dot with Tunable Barriers. *Nano Lett.* **12**, 469–472 (2012).
 - ³¹ Paudel, H. P. & Leuenberger, M. N. Optical selection rules for electron-hole pair excitation in 3D topological insulators. preprint: <http://arxiv.org/abs/1208.4806>.
 - ³² Yusheng, H. & Grassie, A.D.C. The electronic band structure of $\text{Pb}_{1-x}\text{Sn}_x$, Te alloys. 111: Implications for the Fermi surface of SnTe. *J. Phys. F: Met. Phys.* **15**, 363-376 (1985).
 - ³³ Sakurai, J. J. Advanced Quantum Mechanics. Pearson Education (2007).
 - ³⁴ Volkov, B. A. & Pankratov. Two-dimensional massless electrons in an inverted contact. *JETP Lett.* **42**, 178 (1985).
 - ³⁵ Abramowitz, M. & Stegun, I. A. Handbook of mathematical functions, p. 443 (Natl. Bur. Std., Washington, 1972)